

THE EFFECTS OF FREE-STREAM TURBULENCE ON FLOW-INDUCED LOADS

Francisco J. G. de Oliveira
Department of Aeronautics
Imperial College London UK
f.oliveira22@imperial.ac.uk

Zahra Sharif Khodaei
Department of Aeronautics
Imperial College London
z.sharif-khodaei@imperial.ac.uk

Oliver R. H. Buxton
Department of Aeronautics
Imperial College London
o.buxton@imperial.ac.uk

ABSTRACT

An analysis of the relationship between different “flavours” of free-stream turbulence (FST) and the developed fluctuating strain/deflections of bluff bodies is conducted. Regardless of the influence of the FST, bluff bodies at sufficiently high Reynolds numbers produce turbulent wakes in which multiple turbulent length/time scales exist concurrently and interact with the body’s structure. This interaction imprints these multi-scale physics onto the structural response. The present analysis aims to provide more insight into how the presence of FST influences and modifies the experienced flow-induced loads on submerged structures exposed to turbulent cross-flows. We conduct concurrent PIV (Particle Image Velocimetry) and strain measurements using fibre optic sensors embedded into the surface of a submerged bluff body structure (cylinder) to measure the fluctuating velocity components u'_i , and the experienced fluctuating strain ϵ' , at different positions across the structure under analysis. The presence of FST increases the magnitude of the fluctuating strain field of a cylinder both before and after the shear-layer separation, representing the direct and indirect influence of FST on a structure. We show that the bluff body’s structural response is mainly influenced by the coherent structures shed, deeming the indirect influence of FST the main contributor to the structural response of the body.

INTRODUCTION

In order to meet the increasing market demand for renewable energy, wind farms often cluster wind turbines within a confined space. The combination and overlap of wakes generated by different wind turbines within a wind farm results in highly turbulent flows through the wind farm. These flows are characterised by high turbulent intensity ($TI(\%)$) and spatially evolving turbulent length scales. Consequently, wind turbines in these clusters are often exposed to intense FST conditions characterised by different $TI(\%)$ and integral length scales (\mathcal{L}) generated by the wakes of neighbouring wind turbines, dependent on the spacing between themselves. Previous studies have associated the presence of FST with increased power generation in wind turbines (Gambuzza & Ganapathisubramani (2021); Wu *et al.* (2020)), sparking interest in wind tur-

bine allocation optimisation for enhanced power extraction. However, within a wind farm, the spacing between wind turbines is usually a trade off between generating the most power per km^2 of allocated space, and exposing wind turbines to unsteady flow regimes that can accelerate fatigue damage on the structure (Thomsen & Sørensen (1999); Tian W. (2019)). Additionally, the increased wake meandering intensity introduced by higher FST conditions may impose more undesired loading events on downstream machines (Gambuzza & Ganapathisubramani (2023)).

FST has been identified as the primary driver of drag variations (Bearman & Morel, 1983), increased vibration, and deflection of submerged structures exposed to a cross-flow (Wang *et al.*, 2019). In addition, FST has also been associated with a modification of the vortex shedding process in the near-wake of bluff bodies (Kankanwadi & Buxton, 2023). Thus, it directly and indirectly influences the experienced fluctuating loads, with the latter related to the vortex shedding modification process, and the former referring to the direct impact of a fluctuating velocity field impinging on the bluff-body. To measure the flow-induced structural response, we employ novel fibre optic Rayleigh backscattering sensors (RBS) (Xu & Sharif Khodaei, 2020), measuring the strain to which the structure is exposed under different dynamical regimes. The development of optical frequency-domain reflectometry (OFDR) technology has enabled the use of fibre optics as RBS to capture fine details of the structural response of bodies exposed to various flow conditions with a finely distributed spatial sensing network. This allows us to extract the flow-induced effects on the structure. In this system, different sections of the fibres are identified by measuring the frequency shift between two backscattered beams of light. Fibre optics are highly sensitive to factors such as induced axial strain and temperature. Consequently, external events lead to localised frequency shifts in the fibres, which can then be correlated with the experienced strain within the structure using predefined strain frequency shift coefficients. For the first time, we couple these measurements with time-resolved PIV, to acquire concurrent information on the local velocity field, and time-varying strain within the wake-generating body.

Exploring the FST turbulence intensity and integral length scale parameter space $\{TI(\%), \mathcal{L}\}$ has proven to be relevant

to the analysis of the entrainment process into the wake of a 2D cylinder. Kankanwadi & Buxton (2023, 2020) explored a broad $\{TI(\%), \mathcal{L}\}$ space, and its impact on the evolution of entrainment into the near, and far wake of a bluff body, having shown that, in the near wake, where large scales remain coherent, \mathcal{L} promotes entrainment, whilst in the far wake, the variability of $TI(\%)$ in the background becomes the dominant parameter. In this work, a similar FST parameter space is explored to determine the relative importance of \mathcal{L} and $TI(\%)$ on the respective loads to which a bluff body is subjected. This is done whilst concurrently interrogating the flow and the structural response of the wake-generating body, allowing us to assess the induced structural effects of different flow events.

METHODOLOGY

To understand the effect of FST on the flow-induced loading events, we have broken down the problem by using a canonical bluff body (cylinder). Experiments will be scaled up to a model wind turbine in future work. The bluff body preliminary experiments were conducted in the water flume of the hydrodynamics laboratory of the Department of Aeronautics at Imperial College London. An acrylic tube with diameter $D = 50$ mm, $l_t = 2.5$ mm wall thickness and $L = 524$ mm length, was vertically assembled in the mid section of the flume, with a 95% body submersion. A schematic of the experimental apparatus used is presented in Figure 1, as well as the respective spanwise location of the PIV fields of view (FOVs), and the relative positioning of the fibre optic sensing network. For the remainder of the manuscript, the Cartesian coordinate system represented in Figure 1 is used, where $[x, y, z]$ corresponds to the velocity components $[1, 2, 3]$ respectively. Upstream of the cylinder, turbulence-generating grids were placed to create background turbulence, allowing us to investigate the effects of $TI(\%) = \sqrt{(u_1^2 + u_3^2)}/2/U_\infty$ and integral length scale ($\mathcal{L}_{13} = \int_0^{r_i} R_{13}(r)dr$) in the free-stream flow, where R_{13} corresponds to the autocorrelation function between $u_1(x, z)$ and $u_1(x, x+r)$, and r_i is the first zero crossing of the autocorrelation function. The incoming free-stream velocity of the flow, without the presence of the turbulence-generating grid, was 0.47 m/s, setting the Reynolds number of the flow based on the undisturbed free-stream velocity and D to $\approx 25,000$. The cylinder was set up as a cantilever, filled with water to neglect buoyancy effects, and the tip of the cylinder was left free to allow the development of tip vortices and the induced downwash (Porteous *et al.* (2014)), recreating free-end and 3D flow structures, approximating the flow to a wind turbine mast.

Simultaneously to the acquired PIV FOV, measurements of the structural strain were conducted. This allowed concurrent capturing of the fluctuating strain field, and the flow structures that yield it. The induced strain field may be directly related to the loads acting on the bluff body, as a result of being directly linked to the structural response of the body to the boundary conditions of the problem. In this case, these consist of the developing flow conditions. The RBS sensors were embedded on the cylinder's surface, capturing the localised strain along its spanwise direction on its windward and leeward faces, along two spanwise polar positions $\theta_f = [45, 135, -135, -45]^\circ$ - see Figure 2. FOV C1 and C2 were overlaid with the fibre optic network location along the cylinder's spanwise direction. The measurements of the acquired strain using the RBS sensors were synchronised with the PIV, both set at an acquisition frequency of 50 Hz. PIV data was captured in a pairwise manner, and so the strain data was

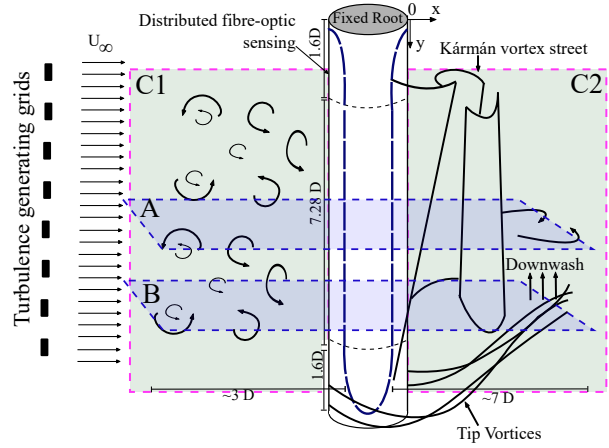


Figure 1. Experimental layout schematic of the fibre optic path, PIV fields of view (FOVs) captured and main flow events over the cylinder.

triggered to acquire between the pair of images comprising the PIV acquisition, over which velocity fields were computed.

The polar angles of the locations of the fibre sensing lines in each face were set to capture the flow events before and after the time-averaged shear-layer separation location (Cicolin, 2021). By measuring the experienced strain on the windward face, onto which FST is incident, and the leeward face we are able to distinguish between the direct and indirect influence of FST on the structural response of the bluff body. The sensing network of RBS possesses a spatial resolution of 2.6 mm where each sensing line consists of 140 sensing points, along $7.28 D$ (364 mm) in the spanwise direction of the cylinder. The sensing network starts at $y/D \approx 1.6$, to decrease the curvature radius of the fibres, thus decreasing the optical losses in the system (Xu & Sharif Khodaei, 2020). These sensors are capable of measuring $\mu\epsilon$ from $[0.1, 1.5 \times 10^4]$. Luna ODISI-B was used as a laser source and acquisition system, and was triggered concurrently with the PIV snapshots by use of an external signal delay generator. The RBS sensors are then used to capture the structural micro strain ($\mu\epsilon$), herein referred to ϵ .

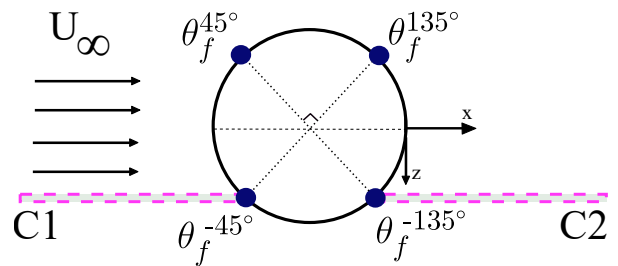


Figure 2. Fibre optic sensing paths' polar positions overlaid with FOV C1 and C2.

We subject the bluff body to a broad parameter space of \mathcal{L}_{13}/D and $TI(\%)$, allowing us to understand which of these contributes more to the fluctuating loads acting on the structure. Figure 3 represents the explored FST parameter space. Due to the large dimensions of the cylinder combined with space constraints of the tunnel, the maximum attained \mathcal{L}_{13}/D was smaller than unity. Future work will delve on exploring the effects of FST with an integral length scale bigger than the cross-section of the structure, where the added flow structures

to the free-stream influence the developing wake globally instead of just acting locally. The Strouhal number is herein defined as $St = f \times D/U_\infty$.

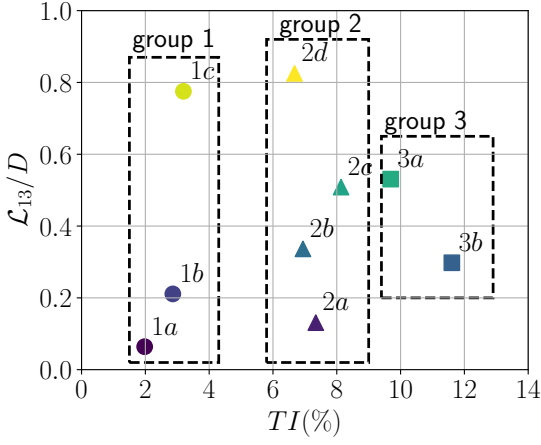


Figure 3. Explored $\{TI(\%), \mathcal{L}_{13}/D\}$ FST parameter space. The different FST conditions were segmented into 3 different groups based on their respective turbulence intensities, to group the effects of \mathcal{L}_{13}/D and $TI(\%)$.

RESULTS AND DISCUSSION

The PIV velocity fields were acquired to capture the developing flow around the bluff body, inducing the loads on the structure. Instantaneous snapshots of the velocity magnitude fields (U) from FOVs C1 and C2, for FST conditions 1a and 2a, are presented in Figure 4. These snapshots demonstrate the inhomogeneous vortex shedding of the bluff body induced by the free-end extremity of the cylinder. The cylinder root region (corresponding to the fixing region of the bluff body) experiences both the strongest intensity of von Kármán vortex shedding in the flow (Porteous *et al.*, 2014), and the largest bending moment. As the acquired strain is directly related to the structural loads to which the bluff body is subjected, the instrumented strain field acquired at the root corresponds to an integration of load events spanning along the extent of the cylinder, acting as a root bending moment.

The presence of FST has been linked to an increase of the vibration of cantilevered bluff bodies (Wang *et al.* (2019)), and the usage of distributed sensing networks allows for a better understanding of the evolution of the structural response of bluff bodies exposed to the said FST. Furthermore, thanks to the concurrent structural and flow data acquired, we can also analyse the fingerprint of the developing flow structures acting on the solid structure. A Reynolds decomposition is applied to the strain signal, extracting the mean ($\bar{\varepsilon}$) and fluctuating (ε') strain field of the body $\varepsilon(y/D, t, \theta_f^\alpha) = \bar{\varepsilon}(y/D, \theta_f^\alpha) + \varepsilon'(y/D, t, \theta_f^\alpha)$. The contour of the spanwise evolution of the probability density function (PDF) of the acquired signal by the sensing lines $\theta_f^\alpha, \alpha = [-45^\circ, -135^\circ]$ is presented in Figure 5. The PDF contour is also overlaid with the mean, standard deviation and maximum|minimum ranges of the acquired strain field for FST cases 1a and 2a. The introduction of FST on the representative case 2a accounts for an increase of the

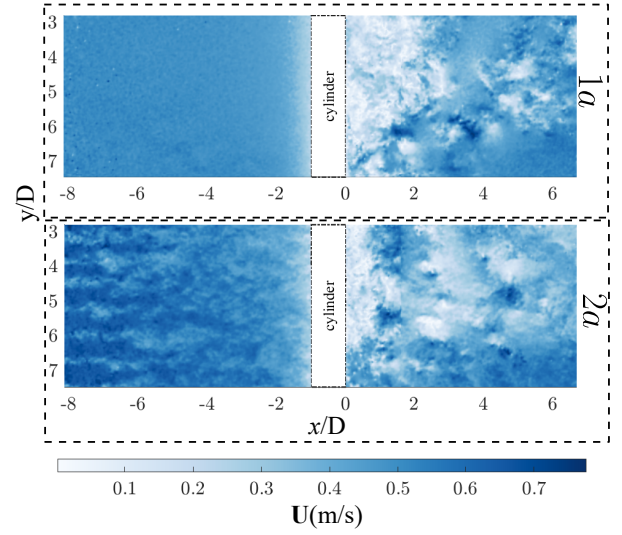


Figure 4. PIV flow snapshots captured in FOV C1 and C2, for FST cases 1a and 2a.

maximum|minimum range of the fluctuating strain, and an increased standard deviation, especially at the root. The PDF of the fluctuating strain also shows an increased kurtosis of the curve as the spanwise coordinate approaches to the root, representative of an intermittent fluctuating stress introduced by an increased vibration of the bluff-body.

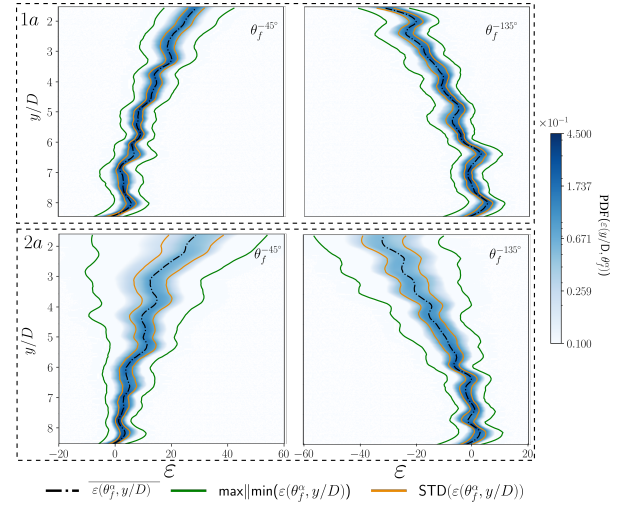


Figure 5. Longitudinal distribution of the PDF of ε across the data retrieved by $\theta_f^{-45^\circ}$ and $\theta_f^{-135^\circ}$. The PDF contours are overlaid with the mean, standard deviation and maximum and minimum limits of strain experienced by the cylinder.

To explore the effect of the introduction of FST on the time-averaged loads experienced by the bluff body, we analyse the time-averaged tip deflection captured by the fibre-optic sensing network along the spanwise direction of the cylinder. In Bearman & Morel (1983), the authors reported that the increase of $TI(\%)$ in the free-stream effectively increased the time-averaged loads acting on the cylinder, directly associated with a decrease in the streamwise extent of the wake's recirculation region and vortex-formation length. To reconstruct the deflection of the bluff body, the following shape sensing

algorithm is employed (Xu & Sharif Khodaei, 2020):

$$\beta_n = \frac{2\Delta L \times \varepsilon_{n-1}}{l_t} + \sum_{j=1}^{n-1} \beta_j \quad (\text{i}),$$

$$\delta_n = \Delta L \times \left(\frac{2\Delta L \times \varepsilon_{n-1}}{l_t} + \beta_{n-1} \right) + \delta_{n-1} \quad (\text{ii}),$$

where β_n and δ_n correspond respectively to the rotation and deflection (δ) of the local sensorised regions. The deflection of each spanwise polar region, instrumented by the fibre optic sensing paths is assessed by computing the local deformation and rotation of the body, and projecting this iteratively along the spanwise extent of the measurement region. The final obtained deflection is an estimate of the real deflection of the body, as the sensing region starts at $y/D \approx 1.6$, but sufficient to compute an estimate of the time-averaged loading difference between the tested FST conditions. The averaged largest deflection for each case over the set of 4 sensing fibres, located at the tip region ($\overline{\delta}_{tip} = \frac{1}{N_{fibres}} \sum_i^{N_{fibres}} \overline{\delta}(t, i, y \approx 9D)$) is presented in Figure 6. This metric provides an estimate of the spatio-temporally averaged loads acting on the cylinder, affecting the mean deformation of the cantilevered cylinder.

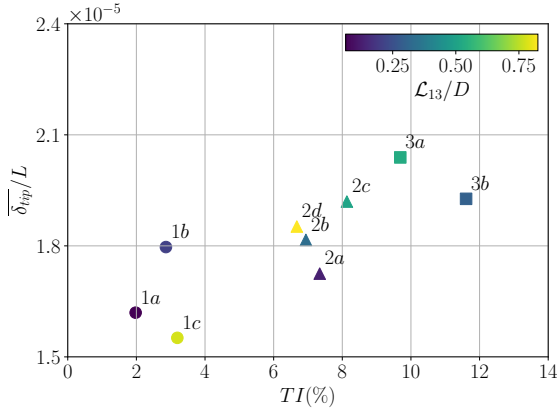


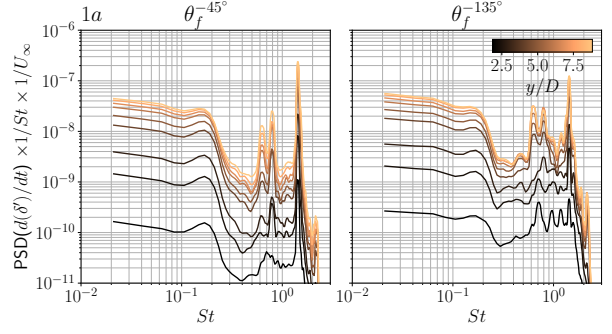
Figure 6. Spatio-temporally averaged free-end deflection of the bluff body for the duration of the conducted tests.

As demonstrated in Figure 6, the increase of $TI(\%)$ results in a positive correlation with the tip deflection of the cylinder, which can be directly linked with an increase in the spatio-temporally averaged loads acting on the bluff body. These results are in accordance with the results reported in Bearman & Morel (1983) for 3D wake-generating bodies.

The frequency-weighted power spectral densities (PSDs) of the normalised fluctuating deflection rate, recomputed from the acquired strain field obtained from θ_f^α , $\alpha = [-45^\circ, -135^\circ]$, for the FST cases 1a and 3a are represented respectively in Figures 7 a) and b), for different positions over the spanwise length of the cylinder. The fluctuation rate of deflection or strain may be linked to a locally induced acceleration on the body, thus related to the induced loads by the flow.

Figure 7 reveals a global increase in the overall “energy” associated with the deflection of the cylinder, as the free-end of the body is approached. As one progresses along the cylinder’s extent towards the free-end of the body, the associated deflection, characteristic of the structural response, reaches

a)



b)

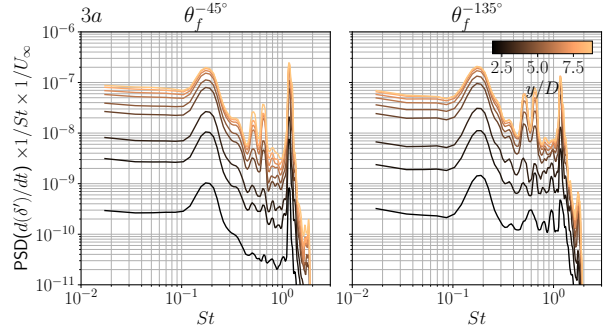


Figure 7. Frequency-weighted PSD of the fluctuating deflection field, obtained through equation (1) for different spanwise positions, along θ_f^α , $\alpha = [-45^\circ, -135^\circ]$, for FST cases 1a and 3a.

bigger amplitudes, culminating in a characteristic larger deflection “energy”. Furthermore, the peak associated with vortex shedding at $St \approx 0.2$ is present in every “energy” spectrum presented, with a relative “energy” increase with the introduction of FST (Figure 7-b)), both captured by the fibres on the leeward and windward face of the bluff body. The associated “energy” increase of the structural response at the characteristic frequency of the vortex shedding reflects the impact FST has on the structural response, induced by these coherent structures shed by the cylinder. This may result from an increased energy associated with it, or to an increase of its spanwise coherence, culminating in an increased effect on the root bending moment experienced by the bluff body. Similarly, Maryami *et al.* (2020) reported an increase in the correlation along the spanwise direction of a 2D cylinder of such flow structures, with the increase of $TI(\%)$ in the free-stream.

The dominant frequencies acting on the structure imposed by the flow, are characterised by analysing the transverse velocity energy spectra acquired by the PIV velocity fields. The energy spectra of the transverse velocity field along the transverse direction of the flow, acquired in FOV A and B for FST cases 1a and 3a, at the streamwise locations $x/D = [0.5, 1.5]$ for brevity are presented as contour plots in Figure 8. Tip vortices and low-frequency flow components, ranging from $St = [2, 10] \times 10^{-2}$ (Hain & Kähler (2008); Porteous *et al.* (2014)), are captured by FOV B, close to the free-end of the cylinder, whilst at the spanwise location of FOV A these structures are less prominent, representing the cellular shedding of the cantilevered cylinder along its spanwise direction. Furthermore, the energy associated with classical shedding is dom-

inant in the central FOV A, with an increase with the introduction of FST, especially in the region close to the cylinder at $x/D = 0.5$. Similarly, FOV B shows an increased energy in the frequency band of classical vortex shedding with the introduction of FST. This confirms the increased spanwise coherence of classical vortex shedding produced by a cantilevered cylinder when FST is introduced. We postulate that this enhanced correlation, together with the increased energy associated with the corresponding flow structures, generates an increased root bending moment on the bluff body.

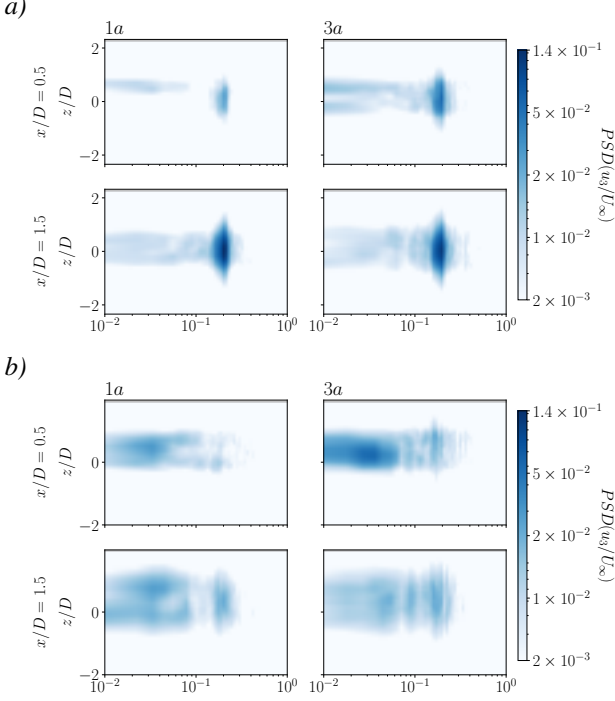


Figure 8. Energy spectra of the normalised fluctuating transverse velocity field for FST cases 1a and 3a, captured in FOV A (a) and B (b), at streamwise locations $x/D = [0.5, 1.5]$.

To quantify the relative energy of the regular vortex shedding process' contribution to the structural response for each of the FST conditions, similarly to Rind & Castro (2012) we define $E^* = (E_{VS} - E_{NOVS})$. This metric allows us to quantify the difference in relative energy from the contribution of vortex shedding to the structural dynamics, where $E = \int_{St_{VS}^-}^{St_{VS}^+} E_{d\epsilon'/dt}(y/D = 1.6) dSt$. Subscripts *VS* and *NOVS* refer to the energy including the peak related to vortex shedding, and without it respectively. In addition, $St_{VS} \pm$ corresponds to the bounding frequencies within the vortex shedding peak. This metric is presented in Figure 9, as a function of $TI(\%)$ in each of the FST cases.

The introduction of FST accounts for an increase in the relative energy of the structural response induced by vortex shedding. Furthermore, Figure 9 shows a positive correlation between the increase of $TI(\%)$ and the increase of E^* . Kankanwadi & Buxton (2023) showed that the length scale of the FST was the most important parameter in affecting the entrainment in the near-wake however our results show that the intensity of the FST is the dominant parameter of the FST that enhances the structural response.

Furthermore, correlations between the flow and the cor-

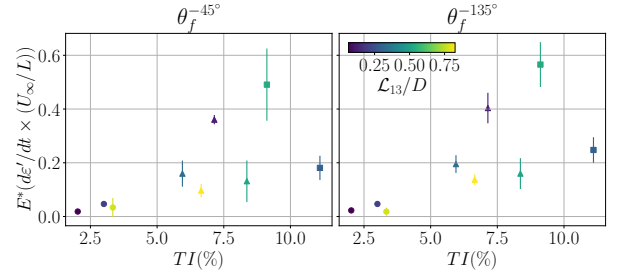


Figure 9. Integration of the PSD of ϵ' over the vortex shedding frequency band.

responding structural response may be performed to analyse how different flow structures are linked to the structural response, and how the previously seen modification of the intensity of such structures affects, and maps into the structural response signal. The influence of the near-wake region of the bluff body and of the free-stream conditions is then assessed, and represented in Figure 10 by examining the cross power spectral density (CPSD) between the normalised strain rate $(d\epsilon'/dt \times U_\infty/L)$ and the normalised fluctuating transverse velocity field u_3/U_∞ along the transverse direction of the flow, at three streamwise stations $x/D = [-2, 0.5, 1.5]$. The strain rate reference signal to perform the CPSDs was extracted from $y/D = 1.6$, representing the start of the strain sensing region, and the effective influence of the flow on the root bending moment, captured by $\theta_f^{-135^\circ}$ for brevity.

The CPSD between the fibre data and the windward flow data is deprived of energy when compared to the CPSD contours obtained downstream of the cylinder, with and without the introduction of FST. Focusing on the data retrieved by FOV A - see Figure 10 (a) -, the introduction of FST also accounts for an increased spatial extent along the transverse flow direction of the correlation between u_3 and the acquired strain rate bending moment signal. Similarly to the PSD of $d\delta'/dt \times 1/U_\infty$, the CPSD frequency band associated with vortex shedding shows a broadening of the energy band in frequency space. Furthermore, the presence of FST accounts for an energy increase in the regular vortex shedding frequency range. This results from the enhanced energy content associated with the flow structure, and from an enhanced spanwise correlation of the developing coherent structures, culminating in an increased bending moment associated with them. Additionally, the introduction of FST accounts for a relative increase in the energy band of both regular vortex shedding and tip vortices at low frequencies captured by FOV B. The introduction of FST accounts for an increase in the intensity of the shed tip vortices from the free-end of the structure, producing an increased energy in this energy band when compared to the case without FST. In summary, the introduction of FST accounts for an increase in both spanwise coherence and the intensity of the vortex shedding, which yields an enhanced structural response as evidenced by the CPSDs.

CONCLUDING REMARKS

A novel technique to instrument the flow-induced loads, and the respective structural response of a bluff body was developed. This was implemented in a conventional cylinder set as a cantilever, approximating the operating conditions of a wind-turbine tower. The combination of temporally-resolved PIV and RBS sensors allows us to exploit the spatial resolution of both methodologies, characterizing how different flow

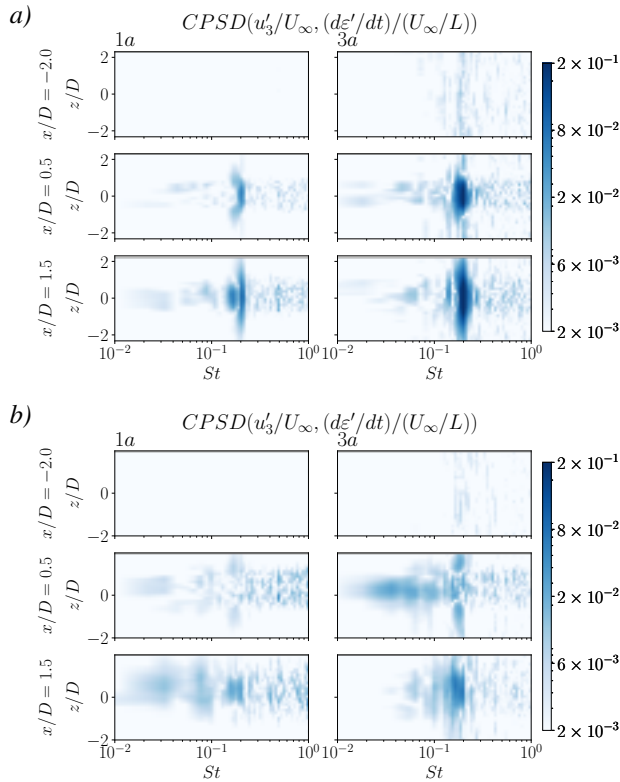


Figure 10. CPSD between u_3/U_∞ acquired by FOV A (a) and FOV B (b), and the strain rate acquired by $\theta_f^{-135^\circ}$ ($y/D = 1.6$), at streamwise locations $x/D = [-2, 0.5, 1.5]$. Only results for FST cases 1a and 3a are shown for brevity.

structures impact on the bluff body. The introduction of FST enhanced the magnitude of ϵ' induced by the root bending moment, and consequently, increased the deflection experienced at the tip of the cantilevered structure. Furthermore, the increase of $TI(\%)$ in the free-stream presented a positive correlation with the time-averaged loads experienced by the bluff-body, similar to the results of Bearman & Morel (1983), who attributed their findings to the modification of the separation points over the bluff body, and a reduction in the spatial extent of the wake. The introduction of FST accounted for an increase in the regular vortex shedding energy in the structural response signal, as well as an energisation of the regular vortex shedding structures shed by the cylinder into the near-wake. In addition, the presence of FST was seen to increase the spanwise coherence of such structures, as seen by the PSD's of the transverse velocity fluctuations at the two different FOV spanwise stations. $TI(\%)$ was seen to be the dominant FST parameter on the growth of the energy of the structural response associated with classical vortex shedding. Furthermore, the CPSDs between the structural response and the flow data showed that the cylinder reacts mostly to the coherent structures shed by the bluff-body, with negligible energy between the incoherent turbulent fluctuations embedded within the free-stream, and the structural response. Thus, the main influence of FST on the aerodynamic loads over bluff bodies is driven by the modification of the vortex shedding process within the body's wake, deeming the direct impact of the induced free-stream veloc-

ity fluctuations negligible. For a cantilevered cylinder, this arises from the combination of an enhanced amplitude of vortex shedding/tip vortices and enhanced spanwise correlation of these flow structures.

Having shown the performance of this new experimental technique, future experiments will be scaled up to a model wind turbine instrumenting the structural response of the turbine's blades, subjecting it to different FST conditions to explore how these affect the dynamic response of the body of the turbine, amidst its operation.

REFERENCES

- Bearman, P. W. & Morel, T. 1983 Effect of free stream turbulence on the flow around bluff bodies. *Progress in Aerospace Science* **20**, 97–123.
- Cicolin, M. M. 2021 Manipulating the flow of a circular cylinder with control rods. Doctor of philosophy, Imperial College London, Aeronautics.
- Gambuzza, S. & Ganapathisubramani, B. 2021 The effects of free-stream turbulence on the performance of a model wind turbine. *Journal of Renewable and Sustainable Energy* **13**, 023304.
- Gambuzza, S. & Ganapathisubramani, B. 2023 The influence of free stream turbulence on the development of a wind turbine wake. *Journal of Fluid Mechanics* **963**, A19.
- Hain, R. & Kähler, C. J. Michaelis, D. 2008 Tomographic and time resolved PIV measurements on a finite cylinder mounted on a flat plate. *Experiments in Fluids* **45**, 715–724.
- Kankanwadi, K. & Buxton, O. R. H. 2020 Turbulent entrainment into a cylinder wake from a turbulent background. *Journal of Fluid Mechanics* **905**, A35.
- Kankanwadi, K. & Buxton, O. R. H. 2023 Influence of freestream turbulence on the near-field growth of a turbulent cylinder wake: Turbulent entrainment and wake meandering. *Physical Review Fluids* **8**, 034603.
- Maryami, R., Aki, S. A. S., Azarpeyvand, M. & Afshari, A. 2020 Turbulent flow interaction with a circular cylinder. *Physics of Fluids* **32**, 015105.
- Porteous, R., Moreau, D. J. & Doolan, C. J. 2014 A review of flow-induced noise from finite wall-mounted cylinders. *Journal of Fluids and Structures* **51**, 240–254.
- Rind, E. & Castro, I. P. 2012 On the effects of free-stream turbulence on axisymmetric disc wakes. *Experiments in Fluids* **53**, 301–318.
- Thomsen, K. & Sørensen, P. 1999 Fatigue loads for wind turbines operating in wakes. *Journal of Wind Engineering and Industrial Aerodynamics* **80**, 121–136.
- Tian W., Ozbay A., Hu H. 2019 A wind tunnel study of wind loads on a model wind turbine in atmospheric boundary layer winds. *Journal of Fluids and Structures* **85**, 17–26.
- Wang, P. *et al.* 2019 Turbulent intensity effect on axial-flow-induced cylinder vibration in the presence of a neighboring cylinder. *Journal of Fluids and Structures* **85**, 77–93.
- Wu, Y. T., Lin, C. Y. & Chang, T. J. 2020 Effects of inflow turbulence intensity and turbine arrangements on the power generation efficiency of large wind farms. *Wind Energy* **23**, 1640–1655.
- Xu, C. & Sharif Khodaei, Z. 2020 Shape sensing with Rayleigh backscattering fibre optic sensor. *Sensors (Basel)* **20**, 4040.